ELSEVIER

Contents lists available at ScienceDirect

Composites Part C: Open Access

journal homepage: www.sciencedirect.com/journal/composites-part-c-open-access





Cure-induced residual stresses and viscoelastic effects in repaired wind turbine blades: Analytical-numerical investigation

Ayush Varshney^a, Daniel Paul^{a,b}, Puneet Mahajan^{a,*}, Leon Mishnaevsky Jr. ^{c,*}

- a Department of Applied Mechanics, Indian Institute of Technology Delhi, New Delhi, India
- ^b Brunel Composites Centre, College of Engineering, Design and Physical Sciences, Brunel University London, London, UK
- ^c Department of Wind Energy, Technical University of Denmark, Roskilde, Denmark

ARTICLE INFO

Keywords:
Scarf patch repair
Residual stresses
Wind turbine blades
Post-repair mechanical behaviour

ABSTRACT

During scarf repair of wind turbine blades, the difference in coefficients of thermal expansion and chemical shrinkage between the original part and the repair patch leads to the development of residual stresses. These residual stresses are detrimental when the repaired composite structures are subjected to operational cyclic loads and affect their post-repair lifetime. This paper uses a hybrid analytical-numerical model to evaluate the residual stresses in a scarf-repaired composite panel. A Prony series-based viscoelastic model is used to describe the material behaviour of the composite undergoing cure to replicate real-life effects more closely. Experiments on the repaired composite samples and numerical simulations on a model of the same are performed to study the post-repair mechanical behaviour. It is found that the damage initiates at the adhesive interface between the scarf patch and the base composite. The resulting debonding and damage to the base composite leads to the failure of the repaired section.

1. Introduction

The focus on sustainable and environment-friendly techniques in recent years has led to increased attention to concepts such as recycling. This is especially noticeable in industries that use modern materials such as polymer composites. The wind energy industry is one such user of large amounts of polymer-based material in the fabrication of large wind turbine blades, hubs, nacelles and other supporting structures. Keeping sustainability in mind, efforts to either reuse or extend the lifetime of these structures as much as possible becomes necessary.

The life cycle of wind turbine blades has several steps, as shown in Fig. 1. The process begins with the manufacturing of wind turbine blades using fibres and a polymer matrix. After the blade has been mounted on an operational wind turbine, it starts degrading due to factors such as fatigue, surface erosion, unexpected external factors and general wear and tear. Blades require regular inspection to ensure they are within stipulated bounds of safety. If any damage is detected, the blade is thoroughly inspected, and any damage found is characterised based on severity. If the damage is not critical, the blade is repaired using tape attachment or scarf patch repair and re-mounted onto the wind turbine to serve an extended life period. If the damage is severe beyond the scope of being repaired, the blade is scrapped. Techniques such as

solvolysis can be used on end-of-life blades to recycle the fibres. Some recent bio-inspired adhesives used to manufacture wind turbine blades can be disintegrated using custom-made solvents, and the recycled parts or fibres can be reused [1].

Extending the original lifetime of a wind turbine blade by performing repair is an excellent method to lower costs and improve sustainability. Repairs are necessary due to various forms of damages occurring during the operation of the wind turbines. Some damages are gradual (for example, strength degradation due to operational fatigue and surface erosion due to rain or dust impact) while others are sudden and catastrophic (for example, lightning strikes). Although the latter type of damage is more concerning and immediate, they are not as common as the former type. Surface erosion is a specifically common issue seen in wind turbine blades, especially in regions with high rainfall and/or dust storms. The leading edge of the rotating blades, which is continuously in contact with the oncoming wind, is particularly susceptible to erosion. The presence of voids further exacerbates the damage by acting as stress concentrators that lead to crack initiation around these voids [2]. Repairing blades with surface and sub-surface damage to restore its properties as much as possible helps in extending their usable lifetime. The most widely used repair techniques are adhesively bonded repairs which include scarf repair [3,4]. Scarf repair is used in wind turbine

E-mail addresses: mahajan@am.iitd.ac.in (P. Mahajan), lemi@dtu.dk (L. Mishnaevsky).

https://doi.org/10.1016/j.jcomc.2024.100521

^{*} Corresponding authors.

blades to ensure smoothness of the surface which is necessary to maintain its aerodynamic shape. The process involves removing the damaged portion by grinding or burring up to a certain depth and then replacing the removed material with a repair patch. The sides of the burred section are tapered up to a predetermined angle. In wind turbine blade repair, either pre-pregs or pre-cut fibre mats/resin system are used and cured by applying heat using a heating blanket [5]. A schematic explaining the steps in this process is shown in Fig. 2. In this, the removed portion of the base composite is replaced by layers of pre-cut fibre mats impregnated with a polymer resin. After the required number of layers are laid, a heating blanket and/or a vacuum bag is used to cure the polymer matrix and thus repair the composite blade.

The scarf angle plays a role in determining the post-repair strength. Lower scarf angles are preferable to obtain better properties after repair [6]. However, this involves removal of a large amount of material during the burring process [7] which is not always feasible while repairing surface damages in wind turbine blades. Improving the repair process to prevent premature failure during the post-repair operation of wind turbine blades is essential since the post-repair mechanical properties depend heavily on the quality of the adhesive joints, interfaces and other interlaminar layers [8]. The repair process introduces residual stresses due to thermal and chemical effects which affect their post-repair behaviour. Numerical modelling provides a fast and efficient way of estimating these residual stresses and assess the post-repair behaviour of composites.

An important aspect of numerical modelling of composites is the proper selection of material models. Although completely cured epoxy may not show significant viscoelastic behaviour, high temperatures and a low degree of cure could result in considerable viscoelastic effects during the cure process. This needs to be included in the numerical model. A study of the viscoelastic behaviour of a commercial epoxy resin is done by Courtois et al. [9]. Relaxation tests are performed using a three-point bending configuration on a dynamic mechanical analysis (DMA) apparatus at different temperatures and degrees of cure. The viscoelastic effect is exaggerated at higher temperatures and lower degrees of cure, thus resulting in greater stress relaxation. Different viscoelastic models have been proposed in literature to predict the behaviour of the material with cure and temperature dependencies

included. Kim and White [10] use a Prony series based viscoelastic model and shift functions from a time-temperature superposition analysis. Courtois et al. [9] use a similar model and compare the results with a creep test for validation. The results in these studies match the experimental data but the model is applicable only for one-dimensional analysis. Gillani et al. [11] derive a numerical framework for the Prony-series based viscoelastic model which can be used in an Abaqus user subroutine. Blanco et al. [12] extend the model developed by Kim and White [10] to a three-dimensional orthotropic problem and predict manufacturing process-induced residual stresses in a composite laminate. It is important to consider these viscoelastic effects for completeness and better modelling of the residual stresses during the curing process.

Although repair of composite panels has been extensively studied in literature, there is limited investigation with geometries specific to wind turbine blade repair. The aim of the current work is to provide a comprehensive framework using a hybrid analytical-numerical model which predicts the polymer cure kinetics and residual stresses during wind turbine blade repair. It improves existing models by including cure- and temperature-dependent viscoelastic effects to the material model. The cure-induced strains in composite panels are experimentally measured using a digital image correlation (DIC) technique with a nonconventional speckle pattern during the cure process itself, which is usually a challenge. The post-repair mechanical behaviour of the repaired composite is analysed using a numerical model which includes a cohesive zone model for the interface and a composite damage model. Experimental tensile tests are performed on repaired composites and the results are used to validate the computational results.

2. Hybrid analytical-numerical model

The hybrid analytical-numerical scheme described in a prior work [5] has been used to predict the post-repair residual stresses in a scarf repair patch. The method involves using an analytical model to evaluate the degree of cure of the polymer during the cure process and a numerical model to predict the residual stresses in the repair patch after cure. The process is shown in Fig. 3. The various models and methods used are explained in the following sections.

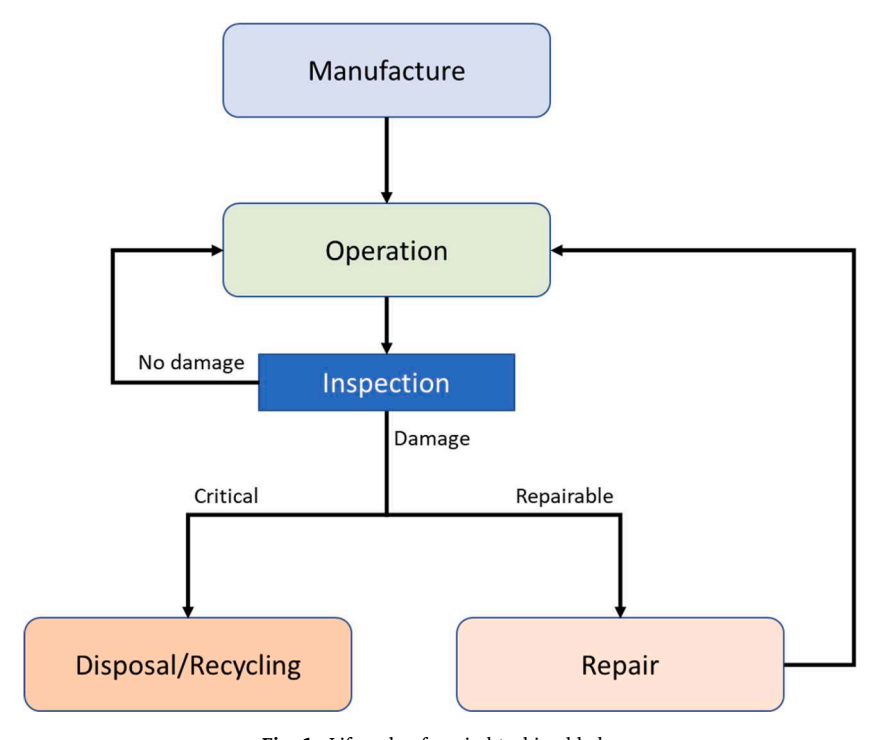


Fig. 1. Lifecycle of a wind turbine blade.

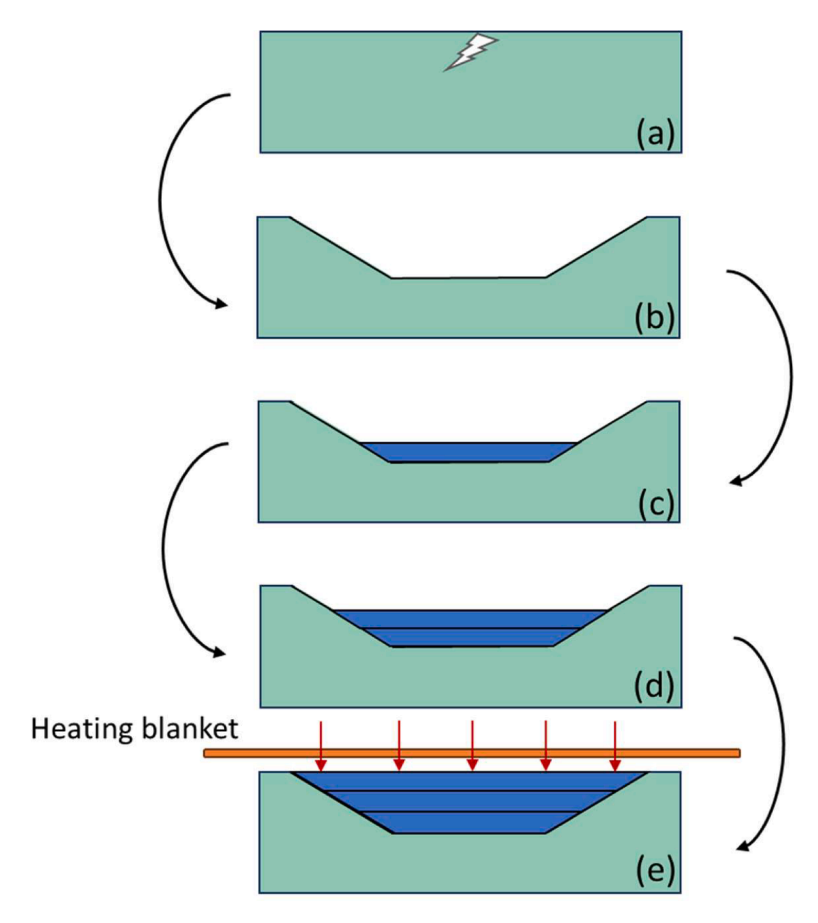


Fig. 2. Stages in the soft patch repair process; (a) The composite with surface or sub-surface damage, (b) The composite with the damaged portion removed by burring up to a certain depth, (c), (d) Fibre mats and resin used to lay up the repair patch layer-by-layer, (e) Repaired composite allowed to cure using a thermal blanket and/or vacuum bag.

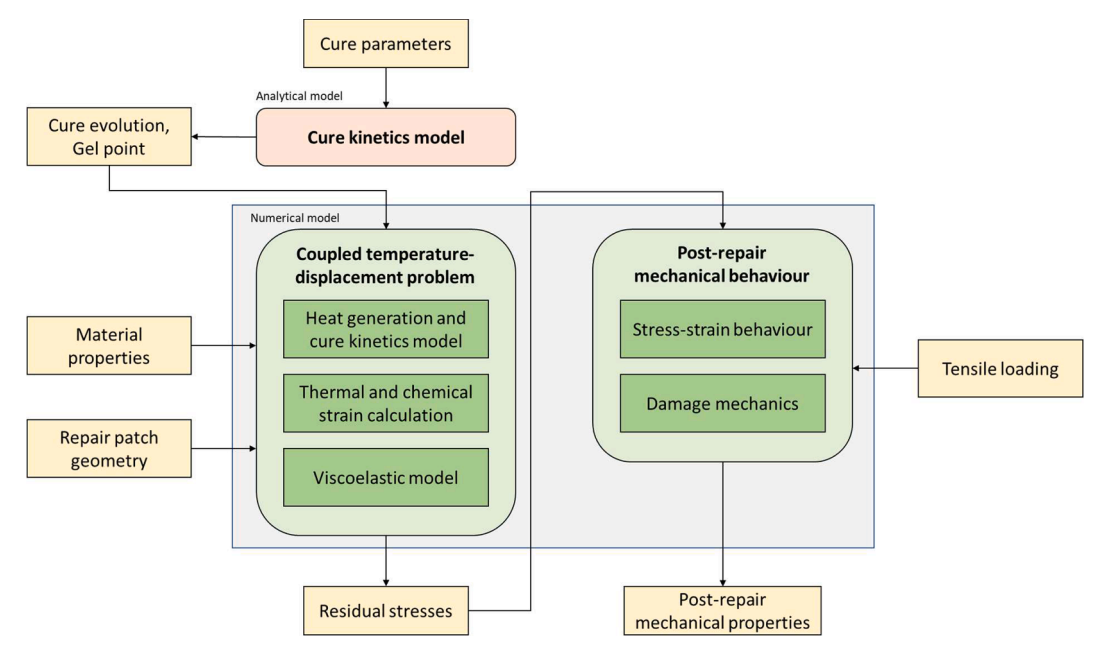


Fig. 3. A flowchart depicting the various steps in the computational scheme used.

2.1. Cure kinetics

The polymer curing process can be quantified numerically in several ways. Empirical kinetic models have been widely used for this purpose.

A summary of the models generally used to describe the cure kinetics of thermoset resins is given by Halley and Mackay [13]. Out of these, several studies ([14,15]) use autocatalytic models to predict and understand the cure behaviour of epoxy resins. The rate of reaction $(d\alpha/dt)$

is described as [14]

$$\frac{d\alpha}{dt} = (k_1 + k_2 \alpha^m)(1 - \alpha)^n \tag{1}$$

where α is the degree of cure, and m and n are model coefficients. The coefficients $k_i (i = 1, 2)$ are functions of temperature and are given as

$$k_i = k_{0i} \exp\left(-\frac{E_{a_i}}{RT}\right) \tag{2}$$

where k_{0i} are model coefficients, E_{ai} are the activation energies (i = 1, 2), R is the gas constant (= 8.314J/K/mol) and T is the current temperature.

The cure kinetics Eqs. (1) and (2) are used in MATLAB to obtain the cure evolution details of the epoxy used subject to different temperature cycles. The cure kinetics parameters are from [5]. Information such as the time to gelation and time to 90 % cure are found and are used in the subsequent steps in the numerical model. The gel point plays an important role in the assumptions made in the numerical model and is the defined as the stage during the cure process characterised by a sudden rise in viscosity and after which resin stop flowing freely.

2.2. Viscoelastic model

A generalised Maxwell model is used in this study to describe the viscoelastic effects. A schematic representation of the model is shown in Fig. 4. The model consists of one free spring element with stiffness Q_0 connected in parallel with a number (N) of 'Maxwell elements' where the ith Maxwell element is a series combination of a spring with stiffness Q_i and a dashpot with damping factor η_i . When this system is subject to a sudden displacement, the springs control the initial stress developed based on their combined stiffnesses. After this initial displacement, holding the displacement of the system fixed causes a gradual decrease of the stresses due to the decaying action of the dashpots until the system reached a steady constant stress called the fully relaxed stress. This process of reduction of stresses called stress relaxation. The equation describing the Maxwell model has one stress term for the first free spring and one additional term for every Maxwell element used. The first term represents either the initial stress (short-term formulation) or the fully relaxed stress (long-term formulation) of the system. The other terms are each defined using a set of two constants for every individual Maxwell element: a weighting factor which decides the stiffness of the spring and a relaxation time parameter which decides the stress decay caused by the dashpot. A long-term formulation with 9 Maxwell elements is used in this study. The formulation for the cure- and temperature-dependence of the viscoelastic model is based on equations in [12].

In the absence of temperature and degree of cure effects, the stresses in an orthotropic composite are given in Eq. (3)

$$\sigma_i(t) = (Q_{ij})_{\infty} \in_j + \sum_{p=1}^{N} (Q_{ij})_p \exp\left(-\frac{t}{\tau_p}\right) \in_j; \ i, j = 1, 2, ..., 6$$
 (3)

where \mathbf{Q}_{∞} is the long-term (orthotropic) stiffness matrix, $\mathbf{Q}_p = w_p \mathbf{Q}_{\infty}$ is the stiffness matrix associated with the p^{th} Prony element, and w_p and τ_p are the weighting factor and relaxation time parameter, respectively.

Defining $(h_i(t))_p$ as the internal stress of the p^{th} Maxwell element and recalling that $\mathbf{Q}_p = w_p \mathbf{Q}_{\infty}$, the stresses developed in a given timestep in which the system is subjected to an incremental strain $\Delta \in$ can be written as

$$\sigma_i(t) = \left(Q_{ij}\right)_{\infty} \in_j + \sum_{p=1}^{N} \left(h_i(t)\right)_p \tag{4}$$

$$(h_i(t))p = \int_0^t w_p(Q_{ij})_{\infty} \exp\left(-\frac{t-s}{\tau_p}\right) \frac{\partial \in_j}{\partial s} ds$$
 (5)

where t and s are the times at the start and end of the current timestep analysed.

Considering the limits of the current timestep to be $[t_n, t_{n+1}]$ and integrating Eq. (5) up to time t_{n+1} , we obtain the following form of the Eqs. (4) and (5) which can be used for the numerical analysis.

$$\sigma_i(t^{n+1}) = (Q_{ij})_{\infty} \in_j(t^{n+1}) + \sum_{p=1}^N (h_i(t^{n+1}))_p$$
 (6)

$$(h_{i}(t^{n+1}))_{p} = \exp\left(-\frac{\Delta t}{\tau_{p}}\right)(h_{i}(t^{n}))_{p}$$

$$+ \frac{w_{p}\left[1 - \exp\left(-\frac{\Delta t}{\tau_{p}}\right)\right]}{\frac{\Delta t}{\tau_{p}}}\left[\left(Q_{ij}\right)_{\infty} \in_{j}(t^{n+1}) - \left(Q_{ij}\right)_{\infty} \in_{j}(t^{n})\right]$$
 (7)

A partially-cured resin system shows greater viscoelastic effect compared to the fully cured resin. This effect of the degree of cure on viscoelasticity is included in the viscoelastic model by modifying the relaxation times associated with the Maxwell elements. The modified relaxation time is given in Eq. (8) [12].

$$\tau_n(\alpha) = 10^{\left[\log\left(\tau_p(\alpha_r)\right) + \left(f(\alpha) - (\alpha - \alpha_r)\log\left(\lambda_p\right)\right)\right]}$$
(8)

where α is the degree of cure, α_r is the reference degree of cure (= 0.98) and $\lambda_p = \frac{\tau_{peak}(\alpha_r)}{\tau_w(\alpha_r)}$. For an epoxy resin system, the definition of $f(\alpha)$ is adopted from [12] as

$$f(\alpha) = 9.1347\alpha^2 + 0.6089\alpha - 9.3694 \tag{9}$$

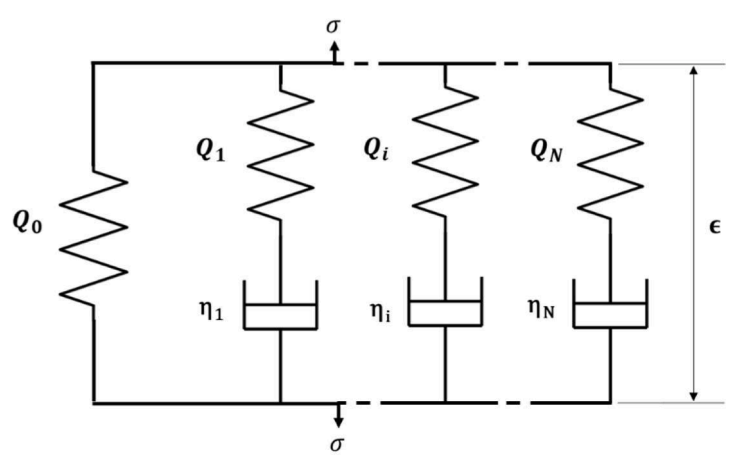


Fig. 4. Schematic of the generalised Maxwell model.

The dependence of the viscoelastic effect on temperature is added to the model by introducing a shift factor, a_T (Eq. (10)), which uses the behaviour of the material at a particular temperature to obtain the behaviour at other arbitrary temperatures. The shift factor is then used to calculate the stresses at a reduced time (ξ) according to Eq. (11).

$$a_T = 10^{\left[-a_1 \exp\left(\frac{1}{\alpha-1}\right) - a_2\right][T - T_r]}$$
 (10)

$$\xi^{t} = \int_{0}^{t} \frac{ds}{a_{T}(\alpha, T)}; \ \xi^{s} = \int_{0}^{s} \frac{ds}{a_{T}(\alpha, T)}; \ \xi^{\Delta t} = \int_{t}^{t+\Delta t} \frac{ds}{a_{T}(\alpha, T)}$$
(11)

where *t* and *s* are the current and previous time steps.

The modified internal stresses which include both temperature and cure dependency are given as

$$\begin{split} \left(h_{i}\left(t^{n+1}\right)\right)_{p} &= \exp\left(-\frac{\xi^{\Delta t}}{\tau_{p}}\right) (h_{i}(t^{n}))_{p} \\ &+ \frac{w_{p}\left[1 - \exp\left(-\frac{\xi^{\Delta t}}{\tau_{p}}\right)\right]}{\frac{\xi^{\Delta t}}{\tau_{p}}} \left[\left(Q_{ij}\right)_{\infty} \in_{j}\left(t^{n+1}\right) - \left(Q_{ij}\right)_{\infty} \in_{j}\left(t^{n}\right)\right] \end{split}$$

However, since the viscoelastic effect in the fibre-dominated directions of the composite is negligible, only the stresses in the matrix-dominated directions of the composite are described using the viscoelastic model while the stresses in the fibre-dominated directions are assumed to be elastic.

2.3. Residual stress analysis model

For this analysis, it is assumed that there is no significant residual stress before the gel point. Subsequent to the gel point, the cure-induced strains and residual stresses are determined by modelling the composite panel cure process in Abaqus. An implicit coupled temperature-displacement step is used for the problem. The details of the heat transfer problem solved, and the formulation of the thermal and chemical strains are provided in an earlier paper [5]. The governing equation for three-dimensional heat conduction is given as

$$\frac{\partial}{\partial x} \left(k_x \frac{\partial T}{\partial x} \right) + \frac{\partial}{\partial y} \left(k_y \frac{\partial T}{\partial y} \right) + \frac{\partial}{\partial z} \left(k_z \frac{\partial T}{\partial z} \right) + \Phi = \rho c_p \frac{\partial T}{\partial t}$$
 (13)

where k_x,k_y and k_z are the thermal conductivities, ρ is the density, and c_p is the specific heat of the composite. Φ is the heat generated by the exothermic cure process and is given as

$$\Phi = V_m \rho_m H \frac{d\alpha}{dt} \tag{14}$$

where V_m and ρ_m are the volume fraction and density of the resin system respectively, H is the heat of polymerisation and $\frac{d\alpha}{dt}$ is the rate of curing. The degree of cure at the beginning of the numerical simulation (the gel point) is given as

$$\alpha(\nu,0) = \alpha_{gel} \tag{15}$$

The heating of the laminate by the heating table is replicated by prescribing a temperature profile (T(t)) to the bottom/upper side of the laminate. The initial condition at any given point (ν) on the laminate is given as

$$T(\nu,0) = T_{gel} \tag{16}$$

where T_{gel} is the temperature of the laminate at the gel point.

A number of user subroutines are used in order to include the various user-defined formulations:

- The cure kinetics and heat generated due to the curing process are computed in the HETVAL subroutine. This involved initialisation and update of the degree and rate of cure, and the estimation of the heat flux due to curing which is included in the heat transfer equation.
- The thermal and chemical strains in the repair patch are calculated in the UEXPAN subroutine using the temperature and degree of cure data at the current timestep.
- The cure- and temperature-dependent viscoelastic model is formulated in the UMAT subroutine. The cure-dependency of the modulus of the part being cured is also included in this subroutine. UMAT takes in the current mechanical and thermal state of the part being cured along with its viscoelastic material properties and calculates the stress field.

2.4. Properties of the materials used

The properties of the unidirectional composite used in the analysis are shown in Table 1.

2.5. Validation of the viscoelastic model

A 9-element Prony series-based viscoelastic model is used for the analysis. The parameters necessary for the model (Table 2) are obtained from literature [10,12] and have been modified to fit the formulation used in the current study.

In order to validate the viscoelastic model, it is compared with an analysis performed by Blanco et al. [12]. The geometry used is shown in

Table 1Thermal and mechanical properties of the glass fibre-reinforced polymer and epoxy used. The engineering constants are used as the instantaneous properties in the viscoelastic model.

Property		Unit	Composite (UD GFRP)	Epoxy	Reference
Density	ρ	kg/m ³	1865	1270	[16,17]
Longitudinal elastic modulus	E_{11}	GPa	34.95	3.4	
Transverse elastic modulus	$E_{22} = E_{33}$	GPa	10.93	3.4	
In-plane Poisson's ratio	$\nu_{12} = \nu_{13}$	-	0.27	0.3	
Out of plane Poisson's ratio	ν ₂₃	-	0.07	0.3	
In-plane shear modulus	$G_{12} = G_{13}$	GPa	2.5	1.31	
Out of plane shear modulus	G_{23}	GPa	5.12	1.31	
Thermal conductivity	k	W/ (m·K)	0.47	0.43	[18]
Specific heat	c_p	J/ (kg·K)	795	1100	
Coefficient of thermal expansion in longitudinal direction	CTE_1	με/Κ	8.6	58	[19,20]
Coefficient of thermal expansion in transverse direction	CTE ₂ = CTE ₃	με/Κ	22.1	58	
Coefficient of chemical shrinkage in longitudinal direction	CCS_1	με	-220	-4975	[21]
Coefficient of chemical shrinkage in transverse direction	CCS_2 = CCS_3	με	-2850	-4975	
Heat release	H	kJ/kg		473.6	[22]
Fibre volume fraction Convective heat transfer	v_f h	- W/ (m ² ⋅K)	0.55 20		[23]
Emissivity	€	-	0.85		[24]

Table 2 Prony series constants used in the viscoelastic model [12]. τ_p and w_p (p = 1, 2, ..., 9) are the relaxation times and weights associated with each of the Maxwell elements in the model.

p	τ_p (min)	w_p	
1	2.92×10^{1}	6.031	
2	$2.92 imes 10^3$	6.747	
3	$1.82 imes 10^5$	8.485	
4	1.10×10^7	11.449	
5	$2.83 imes 10^8$	15.743	
6	7.94×10^{9}	26.783	
7	1.95×10^{11}	18.809	
8	3.32×10^{12}	5.009	
9	4.92×10^{14}	2.556	

Fig. 5(a). It consists of a four-layered $[0/90]_s$ composite of which a quarter model is analysed. The mesh size and properties are kept the same as that in the paper. The node at [0,0,0] is fixed while the x=0 and y=0 planes are kept symmetric in the x and y directions, respectively (Fig. 5(b)). The temperature cycle applied is depicted in Fig. 6(a). The comparisons of the results of the current model those from the earlier paper are shown in Fig. 6(b) to (d). The strains and stresses at the end of the curing process are found to be comparable.

3. Determination of cure-induced strains in composites panels

This section describes the experimental and numerical methods used to determine the cure-induced strains in composite panels. The comparison of the results enables the determination of the chemical shrinkage coefficient for the resin system under study.

The composite laminate is fabricated by a Vacuum Assisted Resin Infusion Moulding (VARIM) process using glass fiber mats and an epoxy resin system. The fibre mats were procured from SAERTEX India Private Limited and are unidirectional with an areal density of 600 gsm. The epoxy resin system consists of Epotec YD585 resin and Epotec TH7257E hardener. The resin and hardener are mixed in a ratio of 100:32 by weight and degassed in a vacuum chamber to remove air bubbles trapped during mixing. Four layers of pre-cut fibers mats (150 mm \times 150 mm) are placed on a customised heating bed which is preprogrammed to supply a specific temperature cycle to cure the composite. The layup used was $[0_2/90_2]$ with a total thickness of 2 mm. After this, the fibres are enclosed within a vacuum film and the degassed resin is infused to impregnate the fibre mats using a vacuum pump. To cure the resin system used in this study, the bed is heated up to 80 °C and held at the temperature for 4 h. After this, it is naturally cooled to room temperature. The fibre volume fraction in the fabricated laminate is 55

During the process of cure, the strains induced in laminates are experimentally determined using three-dimensional digital image

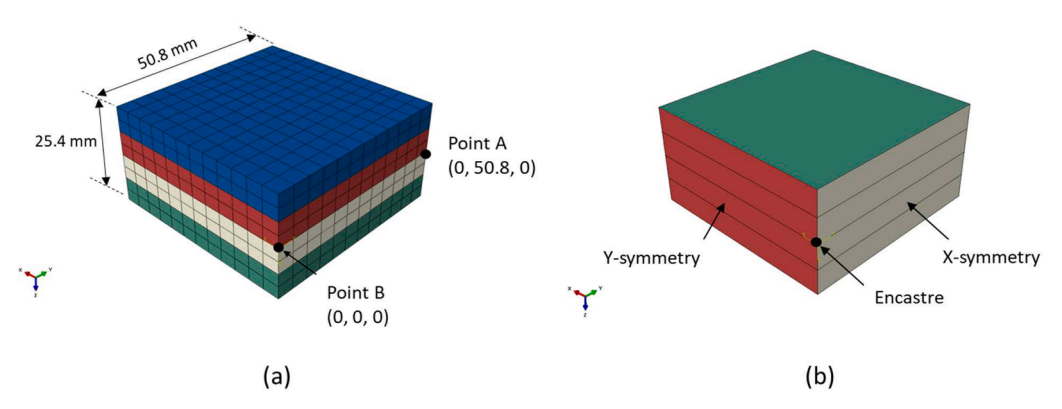


Fig. 5. (a) Model used for validation. (b) Boundary conditions used in the model.

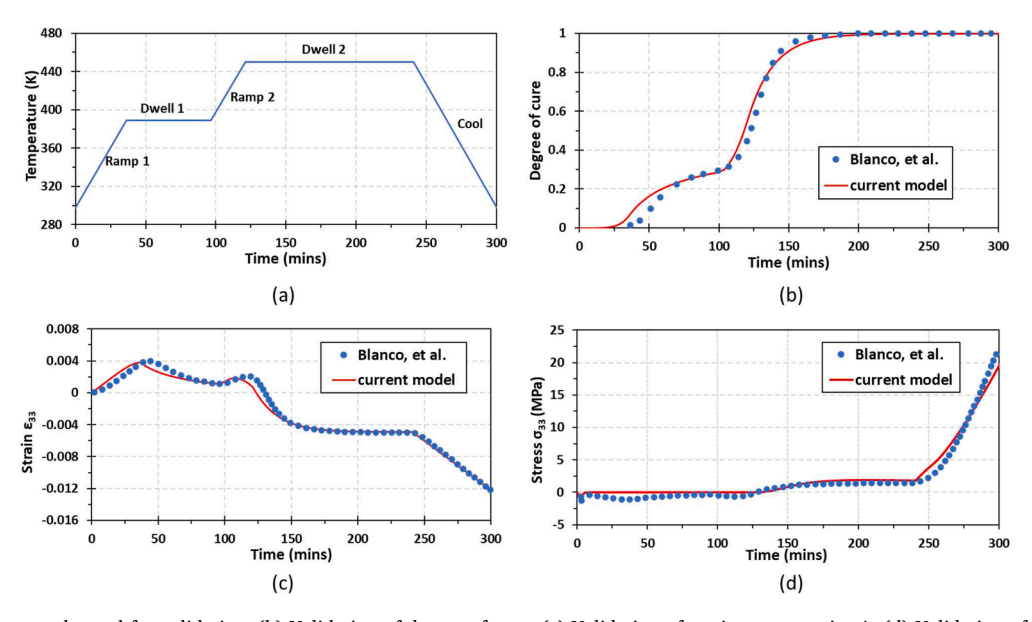


Fig. 6. (a) Temperature cycle used for validation, (b) Validation of degree of cure, (c) Validation of strain \in 33 at point A, (d) Validation of stress σ_{33} at point B; Current model vs. Blanco et al. [12].

correlation (3D-DIC). DIC is a non-contact optical technique to measure strains based on image processing. This technique has been used in the past to measure strains during fabrication of composites, for example, the cure-induced strains in a carbon fibre prepreg composite [25]. DIC requires a speckle pattern on the surface of interest which is tracked by the software at every frame during deformation and correlating the position of subsets with an initial reference pattern to measure the whole-field strain evolution. The speckle pattern is generally created on the specimen's surface using black and white spray paint. However, generating a speckle pattern on a laminate undergoing curing is a challenging task due to the semi solid state of the resin. To address this, powdered black pepper is used here which serves as the black dot pattern while white dye is mixed into the resin being cured to establish a white background similar to the method used by Chen et al. [26]. The speckle pattern on a laminate is shown in Fig. 7.

A photograph of the equipment used for this purpose is shown in Fig. 8. The setup includes two monochromatic cameras (FLIR BFS-U3-120S4M-CS), each with a spatial resolution of 4000pixels \times 3000pixels, equipped with Tamron lenses (23FM50SP) having a focal length of 50 mm. Images are taken every two minutes using a commercial software (VIC-snap) during the temperature hold and cooling phase of cure process. The speckle pattern images are processed using image correlation software VIC-3D, and the strains developed in the laminate during the cure process are obtained.

The evolution of cure-induced strains in a composite panel obtained experimentally is plotted with respect to time in Fig. 9. The plot shows the strains only after gel point as the strains prior to gelation are negligible and the resin can flow freely. There are two distinct regions in the figure. The first is the phase where the temperature is held constant at 80 $^{\circ}\text{C}$ and there are no thermal strains. The only source of strains is chemical shrinkage of the resin. After the hold phase, the composite panel is allowed to cool to room temperature naturally which results in both thermal strains and chemical shrinkage to occur. This manifests as a considerable drop in the total strain, as shown in the plot. The nonlinearity in the strain evolution in this phase is due to the cooling occurring naturally. The speed of cooling depends on the ambient temperature.

The experimental setup described above is simulated using the hybrid analytical-numerical model described in Section 2. The geometry and layup sequence of the laminate is the same as in the experiment used to measure the cure-induced strains and is shown in Fig. 10.

Fig. 11 shows the boundary conditions applied to the model. The prescribed temperature is applied to the bottom surface of the laminate

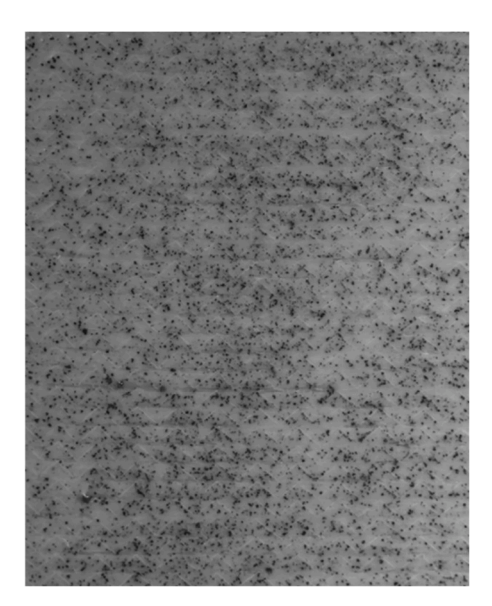


Fig. 7. Speckle pattern made by black pepper.

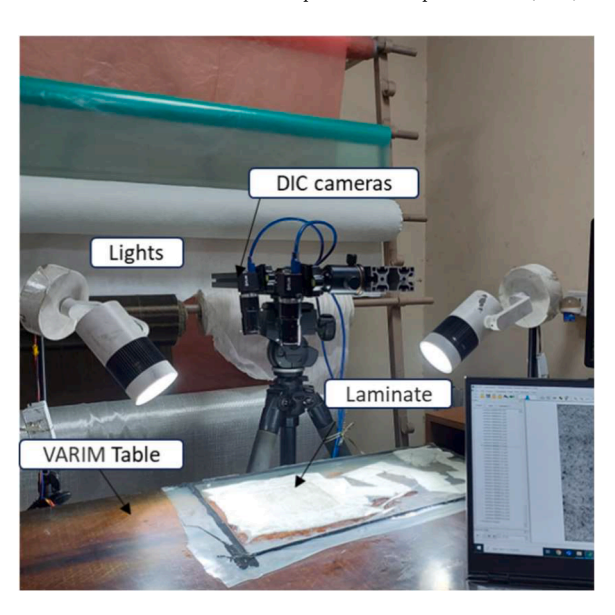


Fig. 8. The DIC setup used for the determination of the cure-induced strains in a laminate.

and replicates the heating bed. All other surfaces undergo heat loss due to convection and radiation. The mechanical boundary conditions are applied such that the motion perpendicular to the bottom surface is restricted since the laminate rests on the heating table in the experiment. Two nodes on the bottom surface: one at the midpoint and another at one of the corners, are restricted to prevent rigid body movement.

Epoxies exhibit a wide range of volumetric chemical shrinkage during cure, varying from 1 to 6 % [27]. This variation impacts the chemical shrinkage coefficients of the composites. In the current study, a comparison of the numerical results with the experimental results is used to determine the chemical shrinkage coefficients of the composite panel during the cure process using a trial-and-error method. The coefficients of the composites in different directions are related to the coefficient of the matrix by the following equations [21]

$$CCS_1 = \frac{CCS_m E_m f_m}{\left[E_{1f} f_f + E_m f_m\right]} \tag{17}$$

$$CCS_2 = CCS_3 = (1 + \nu_m)CCS_m f_m - \nu_{12}CCS_1$$
 (18)

Here CCS_2 and CCS_3 represent the coefficients of chemical shrinkage in the transverse direction, while CCS_1 corresponds to the longitudinal fiber direction. Additionally, v_m is the resin Poisson's ratio, f_m and f_f are the volume fractions of the matrix and fiber, respectively, E_{1f} and E_m are the longitudinal Young's modulus of the fibre and the matrix, and CCS_m is the chemical shrinkage coefficient for the matrix.

All other parameters being known, the chemical shrinkage coefficient of the matrix is varied until the strain evolution obtained using the numerical model closely matches that obtained from experiments. The final strain evolution computed numerically is compared with the experimental results in Fig. 9. The coefficients of the matrix and composite used are shown in Table 1.

4. Determination of post-repair residual stresses in repaired composites

The procedure used to obtain the residual stresses in a scarf repaired laminate is the same as that used in the previous section on a neat laminate, although the geometry is different. A representative cross-section of a repaired part showing the various layers is shown in Fig. 12. A thin adhesive layer between the base composite being repaired and the repair patch causes discontinuity between the fibres in the two

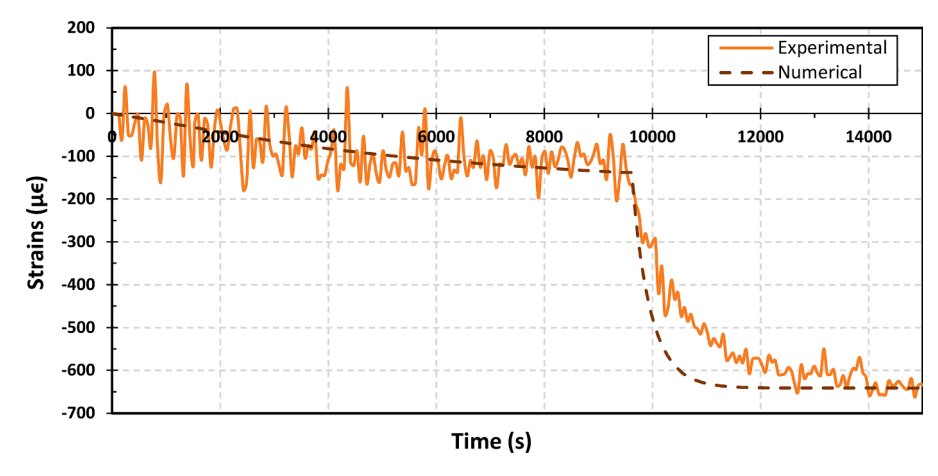


Fig. 9. Comparison of experimental value of strain in cross ply laminate with numerical results.

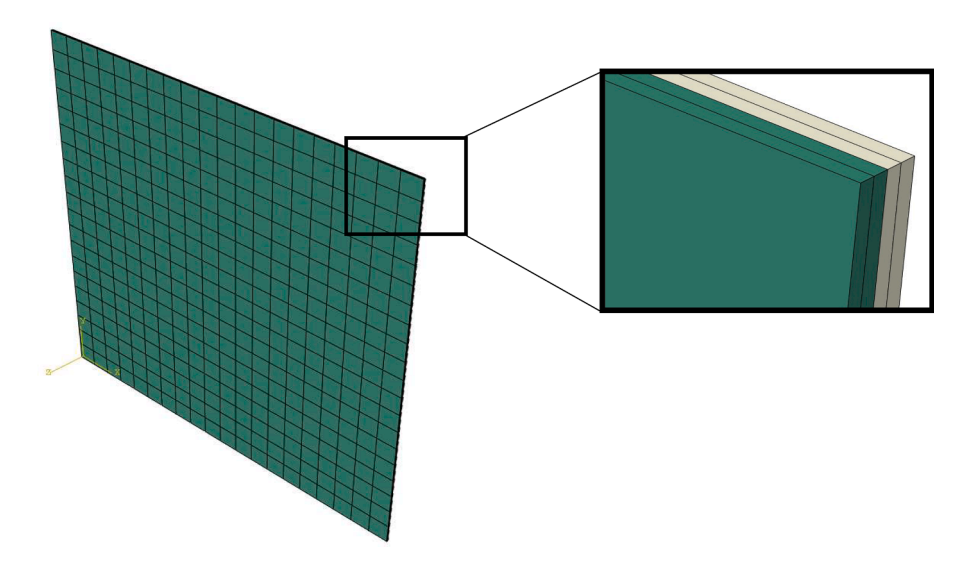


Fig. 10. The model of the laminate $[0_2/90_2]$ used to estimate the cure-induced strains.

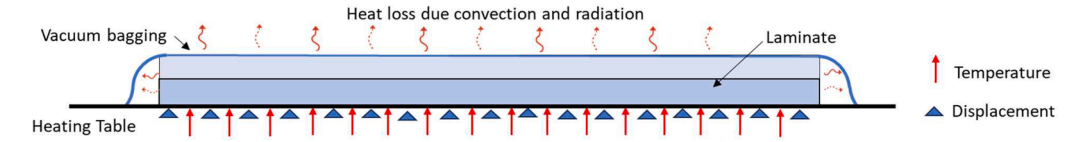


Fig. 11. The boundary conditions applied to the laminate used to estimate the cure-induced strains.

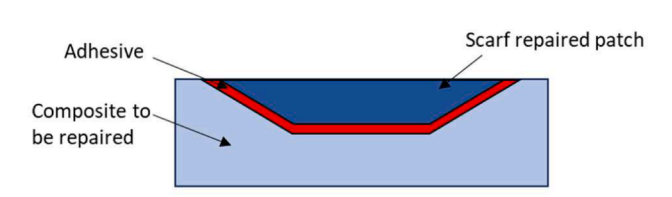


Fig. 12. Scarf patch repair.

sections and is included in the modelling of the repaired part.

A schematic of the laminate geometry model is given in Fig. 13. It consists of the base composite, which has been burred and chamfered, and a square repair patch. The model has a base laminate consisting of 6 plies each being 0.5 mm thick and 300 mm \times 300 mm in size. The central 150 mm \times 150 mm portion of this laminate is considered to the be the damaged section and burred up to a depth of 1.5 mm

corresponding to a thickness equivalent of 3 plies. An adhesive layer of 0.1 mm is modelled between the patch and burred section. The adhesive layer can be seen between the patch and base laminate in composites repaired by the scarf repair process [28]. This means that the repair patch and adhesive layer fits in the burred section and takes the same scarf angle and a size of 150 mm $\, imes\,$ 150 mm. A cross-sectional view of the plies and the repair patch is shown in Fig. 13(b). However, to reduce the computational time, a quarter model of the repaired laminate showed in Fig. 13(a) is used in the numerical analysis. The quarter model used, and the symmetrical boundary conditions applied at its faces are shown in Fig. 14. The quarter model is meshed using a total of 1,73,972 elements of type C3D8T. Among these, 29,104 elements are in the scarf patch. In the C3D8T element type, 'C' denotes continuum, '3D' signifies three-dimensional, '8' represents an eight-noded hexahedral element, and 'T' indicates the inclusion of temperature degree of freedom.

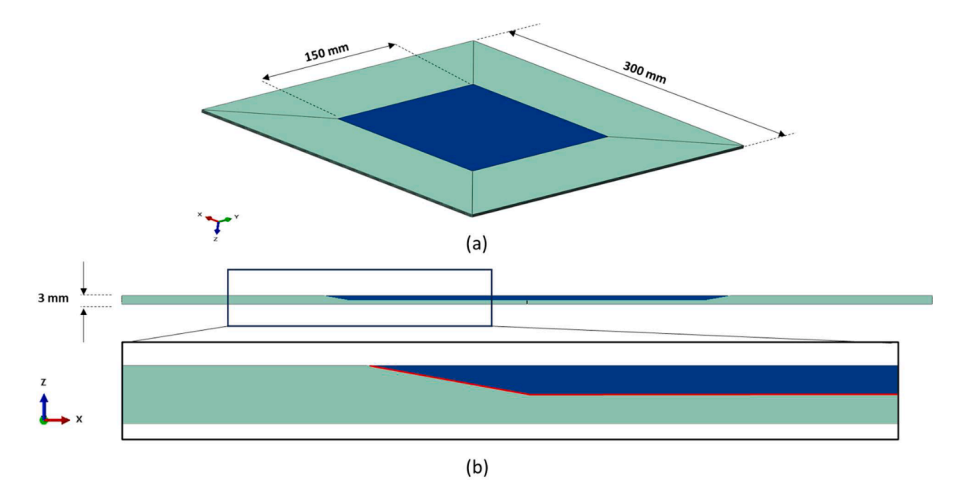


Fig. 13. (a) The geometry of the model used in the residual stress analysis of repaired composite laminates. (b) A cross-sectional view of the model.

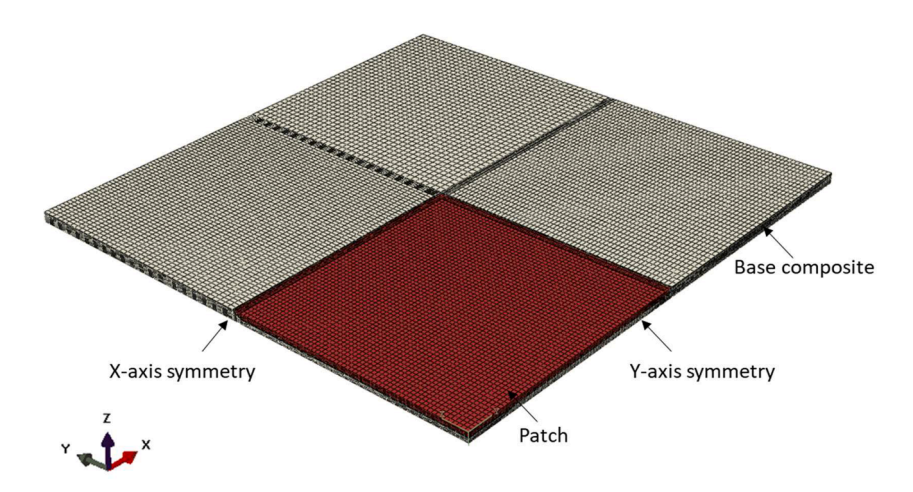


Fig. 14. Quarter model used in the analysis.

Similar to the model to determine the cure-induced strains in laminates, a hybrid analytical-numerical model is used. After obtaining the degree of cure evolution of the resin analytically, coupled temperaturedisplacement steps depending on the temperature profile along with the user subroutines are used in Abagus to estimate the residual stress in the repaired laminate model. The boundary conditions applied are shown in Fig. 15. While the mechanical boundary conditions are the same as that in the composite laminate model (the bottom surface restricted from vertical displacement and two nodes fixed to prevent rigid body motion), the prescribed temperature is applied to the top surface in the case of the repaired laminate model to replicate the effect of the heating blanket. Various single- and two-ramp temperature cycles are studied. Representations of the cycles are shown in Fig. 16. Both the cycles have an initial ramp from room temperature to the first dwell temperature. The single-ramp cycle maintains the temperature at this stage up to a predetermined degree of cure (a value of 90 % in this study). The tworamp cycle, on the other hand, maintains the first dwell temperature

only up to the gel point, after which it is further ramped up to the second dwell temperature. This temperature is then held constant till a degree of cure of 90 % is achieved. After this, the temperature is brought down to room temperature (assumed to be 25 °C) in both the cases at a rate of 2°C/min. For the sake of simplicity of the model, natural cooling is not considered as this would make the temperature drop nonlinear. The temperature profiles for the various cases studied having different dwell temperatures is obtained using the analytical cure kinetics model. However, considering the assumption that the residual stresses are only generated after the gel point reduces the portions in the cycles for which the numerical analysis has to be performed. Thus, the residual stresses analysis for the single ramp consists of only two phases: the dwell phase (BC) and the cooling phase (CD). Similarly, the analysis of the two-ramp cycle considers only three phases: the ramp between the second heating phase and the second dwell phase (CD), the second dwell phase itself (DE) and the cooling phase (EF). In this study, the dwell temperatures are taken to be various combinations within the range of 60 $^{\circ}$ C to 100 $^{\circ}$ C.

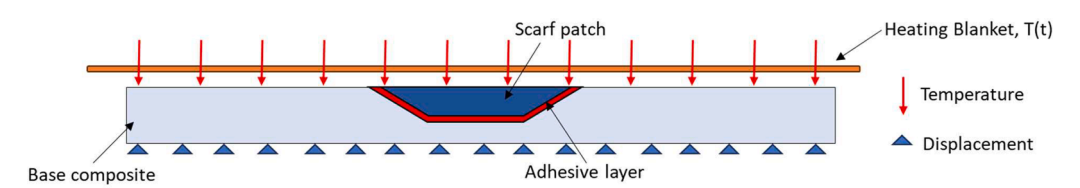


Fig. 15. The boundary conditions applied to the scarf patch repair model.

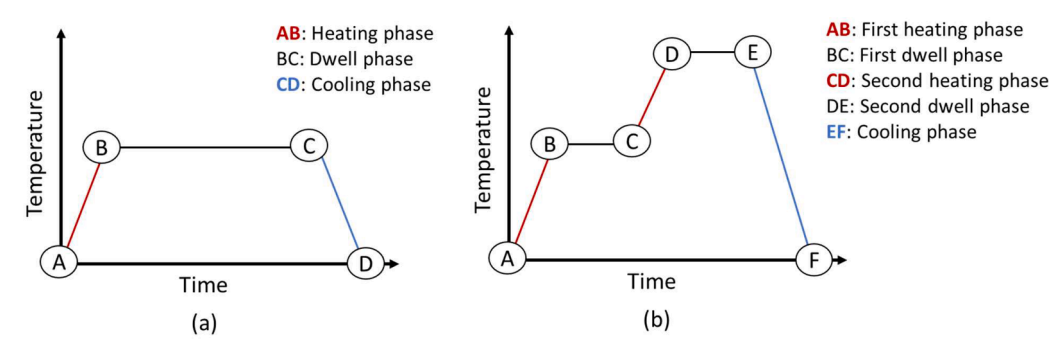


Fig. 16. (a) The single-ramp temperature cycle (b) The two-ramp temperature cycle.

A mesh convergence analysis is conducted to determine the optimal mesh size for residual stress evaluation in the model. Five mesh sizes 4.8 mm, 2.4 mm, 1.2 mm, 0.9 mm, and 0.6 mm are considered the total number of elements being 23,576, 57,152, 173,972, 241,532 and 442,481, respectively. The processor used is Intel Xeon Gold 6254 CPU @ 3.10GHz with 36 cores. An element size of 1.2 mm is found to be sufficient to achieve accurate results while avoiding significant computational costs. Fig. 17 shows the stresses and computational time with element size.

The results of the cure kinetics model for the single- and two-ramp temperature cycles studied are tabulated in Table 3. As expected, the time to gelation and time to 90 % cure are found to reduce with an increase in cure temperatures. This is due to the resins undergoing cross-linking more rapidly at higher temperatures. This leads to more exothermic heat being produced which further accelerates the reaction by a cascading effect.

The post-repair residual stresses in the scarf repair model are next computed numerically for the temperature cycles. The model incorporates viscoelastic behaviour, which varies with both cure and temperature, to achieve more realistic results. Viscoelastic effects are particularly significant at low cure levels and high temperatures, conditions typically close to the gel point, where the adhesive exhibits a more fluid-like behaviour leading to significant stress relaxation [10]. As the adhesive cures, the viscoelastic effect decreases, leading to the development of more pronounced residual stresses. Adding viscoelastic behaviour to the models has a considerable effect on the residual mises stresses in the matrix-dominated directions and the stresses reduce by around 20–40 %. The fibre-dominated direction shows a considerably less change since it is assumed to be elastic and has no direct viscoelastic

Table 3Time to gelation and 90 % cure for epoxy subjected to different single- and two-ramp temperature cycles.

First dwell temperature °C	Second dwell temperature °C	Time to gelation min	Time to 90 % cure min
60	_	215.83	911.44
80	_	66.80	224.34
100	_	42.28	84.09
60	80	215.83	378.09
	100		270.63
80	100	66.80	113.00

effect. Figs. 18 and 19 show the stress evolution in the matrix-dominated direction of an element in the adhesive layer for the single-ramp and two-ramp cases, respectively. In the case of a single-ramp cycle with a dwell temperature of 100 °C (Fig. 18), the stage immediately after the gel point (dwell phase) where viscoelastic effects are pronounced results in lesser stress development when viscoelasticity is considered. The stresses are tensile in nature since they are opposed to the chemical shrinkage occurring, which is the only source of strains in this stage. The cooling phase results in an increase of the stresses and the final residuals stresses obtained from the analysis with the viscoelastic model are lower than the analysis with the elastic model. The residual stress analysis of the two-ramp temperature cycle with dwell temperature of 80 °C and 100 °C (Fig. 19) begins with the heating ramp from the first to the second dwell phases. Thus, in contrast to the stress evolution in the single-ramp case, compressive stresses are observed initially in the analysis with the elastic model due to the effect of the positive thermal

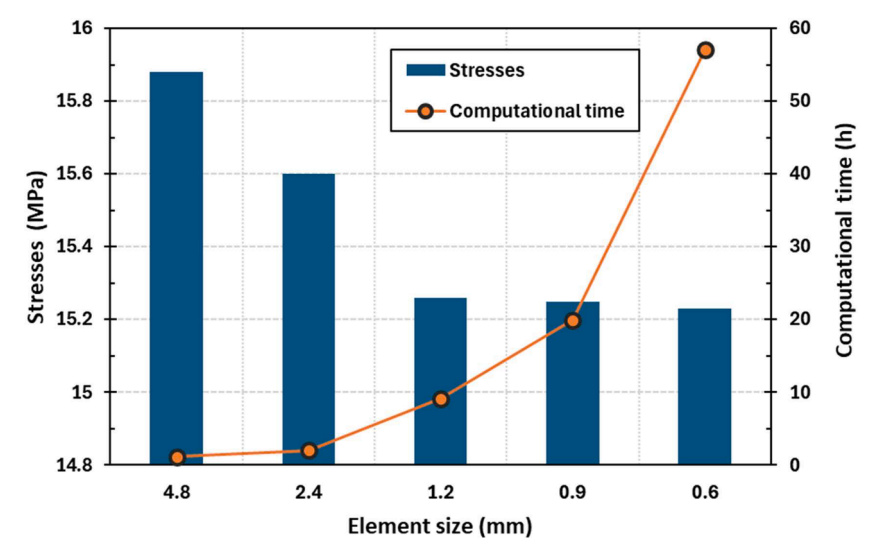


Fig. 17. Stresses and computational time with element size.

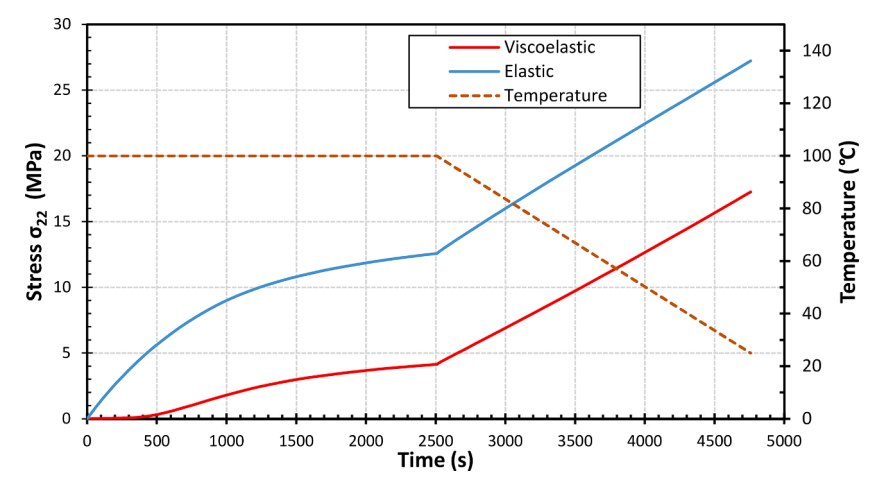


Fig. 18. Evolution of σ_{22} at an element in the repair patch for the 100 °C single-ramp cycle.

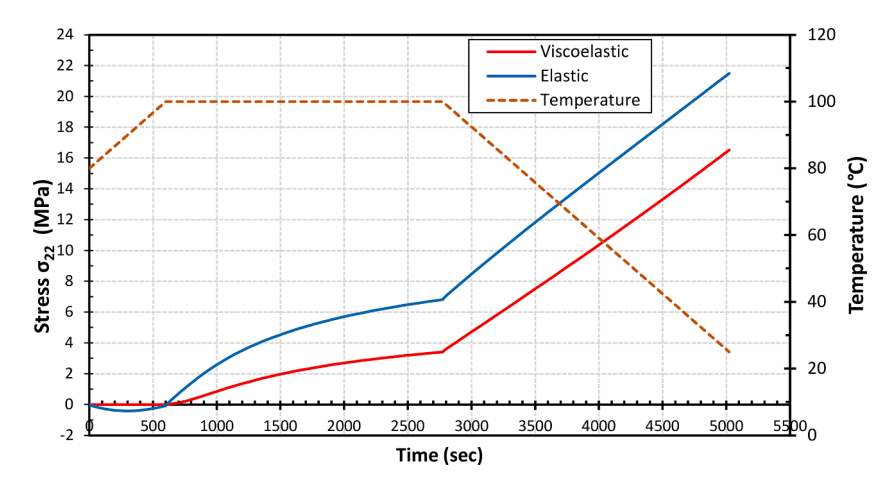


Fig. 19. Evolution of σ_{22} at an element in the repair patch for the 80 °C/100 °C two-ramp cycle.

strains in addition to the chemical shrinkage strains. The second dwell and cooling phases however reverse the stress direction leading to the final residual stresses being tensile. If viscoelasticity is considered, the stresses developed just after the gel point are less prominent compared to the elastic model. It should be noted here that the final residual stresses predicted using the viscoelastic model strongly depend on the curing parameters, particularly, the dwell temperatures. Therefore, each case needs to be properly modelled and analysed.

Table 4 shows the maximum residual stresses estimated using the model for the various temperature cycles studied. Higher cure temperatures lead to a higher residual stress in the repaired composite. The distributions of the stresses in one of the matrix-dominated directions (σ_{22}) in the repaired section after the end of each phase of (dwell and cooling) are depicted in Fig. 20 for the 100 °C single-ramp case. The insets show magnified images of the stress distribution around the interface of the base composite, the repair patch and the adhesive close

to the ends of the patch for each case. The maximum final residual stresses after complete cure are seen to develop in the adhesive layer (Fig. 20(b)) although the maximum stresses in the model occur in other portions like the repair patch at other stages in the process (Fig. 20(a)).

One of the in-plane stresses on the top surface of the model is plotted along the path shown in Fig. 21(a) to study the stress distribution across the interface. The path starts from the middle of the patch to one of the edges of the base composite and passes through the repair patch, adhesive layer, and base composite. The stress distribution along this path is shown in Fig. 21(b). The base composite experiences only thermal strains, whereas the patch and adhesive layer also undergo additional chemical shrinkage. This difference in the thermal and chemical shrinkage coefficients of the composite and adhesive is responsible for the sudden increase in-plane stresses in the adhesive layer. The presence of residual stresses in the base composite/repair patch interface makes it the weakest point when any repaired composite part is re-introduced

Table 4Maximum post-repair residual stresses in different directions in the model for the different cases studied.

First dwell temperature $^{\circ}C$	Second dwell temperature	S11 MPa	S22	S33	S12	S13	S23
60	Single ramp	12.4	12.29	4.383	3.151	1.469	2.401
80	Single ramp	16.97	16.15	5.752	3.648	1.766	2.82
100	Single ramp	21.15	19.78	7.001	4.221	2.22	3.2
60	80	16.6	15.71	5.596	3.504	1.702	2.702
1	100	20.28	18.9	6.651	3.923	2.189	2.958
80	100	20.51	19.11	6.727	3.975	2.203	2.994

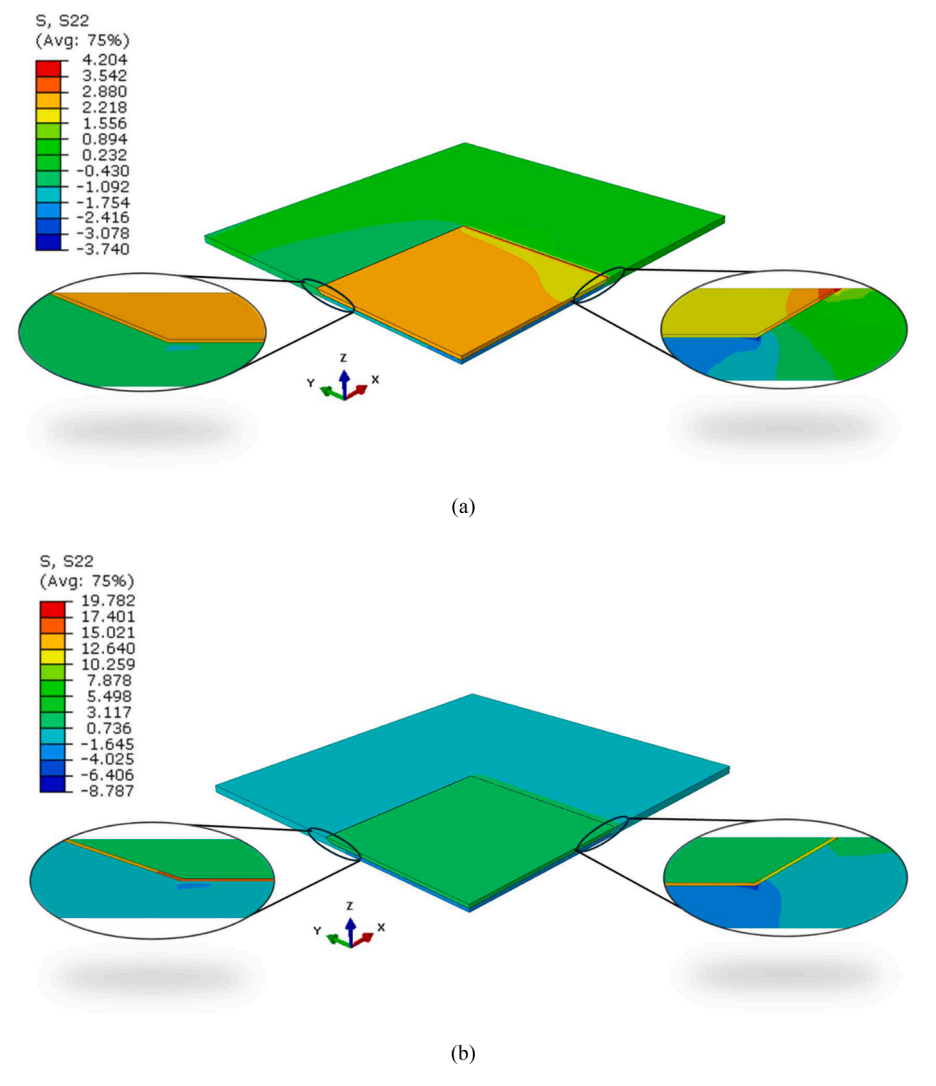


Fig. 20. Stress distribution in the repaired section for the 100 °C single-ramp cycle after (a) dwell phase (b) cooling phase.

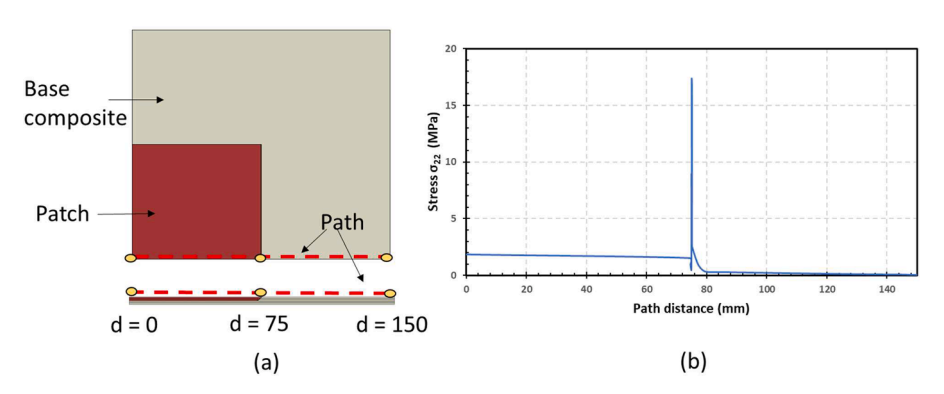


Fig. 21. (a) Path used to plot the in-plane stresses. (b) Stresses along the path.

into cyclic or other complex operational conditions and could lead to failure of the part.

5. Post-repair mechanical behaviour of repaired composites

The composite laminates which are used as the base composite for the scarf patch repaired tensile samples are fabricated according to the method described in Section 3. The composites have six plies laid unidirectionally with a total thickness of 3 mm. Sections measuring 80 mm

 \times 250 mm are cut from the laminate using a water jet-cutting machine. To replicate the burring process in actual wind turbine blade repair, material is removed from the laminate section measuring 40 mm \times 60 mm with a milling machine up to a depth equal to the thickness of three plies i.e. 1.5 mm. Pre-cut fiber mats of the same size are laid in the burred section and impregnated with the resin using a hand layup process to represent the repair patch. Vacuum bagging is performed to remove any excess resin, and the assembly is placed on a heating table at 80 $^{\circ}\text{C}$ for 4 h. In initial trials, a larger repair section was used and

samples with a width of 15 mm were cut and used to conduct the tensile tests. However, these narrower samples were not entirely representative of the behaviour of a scarf repaired section of a wind turbine blade since the residual stresses in the cut sides of the samples would relax upon cutting. To avoid this, the entire repaired laminate of width 80 mm is used to perform tensile tests to investigate its behaviour after repair. Emery cloth strips of length 55 mm are used at both ends of the tensile specimens in the area which is gripped by the jaws of the tensile test machine to ensure the samples do not slip.

The post-repair mechanical behaviour of the repaired composites is investigated next by performing tensile tests with an Instron universal testing machine with a 300 kN load cell at a constant crosshead rate of 2 mm/min. A speckle pattern is applied to the back surface of the tensile specimen for strain measurements using 3D digital image correlation (DIC). The machine has grips measuring 100 mm, suitable for the tensile samples with a width of 80 mm. Two cameras placed at specific angles capture the speckle pattern from two directions during the test and the images are used in the 3D DIC software to obtain the strain evolution. Fig. 22 shows photographs of a sample used for the tensile test and the sample in the UTM during the test.

The failure patterns and mechanical behaviour of the repaired composites under tensile loading is examined thoroughly. An image of one of the samples after performing the tensile tests is shown in Fig. 22 (b). The image shows extensive damage along the length of the sample in the cross-sectional area occupied by the repair patch. The initial damage is seen to occur in the interface between the repair patch and the base composite on the surface of the samples which then propagates along the interface leading to the patch not bearing any further loads. The base composite then fails in the region of reduced cross-sectional area. The stress-strain curves obtained are shown in Fig. 23. The average failure stress of the repaired laminate samples is 329 MPa which is 50 % of the failure stress of a neat composite sample. The low repair efficiency is due to the higher scarf angle used in this study. [6] reports a repair efficiency of 66.5 % for repaired composites with a scarf angle of 5.8° It was not possible to use lower scarf angles in this study since a lower angle requires removal of material over a large area and therefore would result in samples with larger widths, which could not be tested due to geometry limitations of the equipment used.

A numerical model is created and analysed in Abaqus to replicate the post-repair mechanical behaviour of the repaired section and to enable

better prediction of the post-repair behaviour of repaired composite sections in wind turbine blades. A 3D exploded view showing the various parts of the modelled sample and its dimensions are shown in Figs. 24 and 25, respectively. A quarter model with symmetry boundary conditions is used to reduce computational time. A total of 1,97,098 C3D8 elements are used out of which 1,49,468 are of base, 32,208 elements of patch and rest of adhesive layer. The area where the patch is bonded to the base composite consists of a tapered region and a flat region. The tapered region is meshed with a finer element size of 0.096 mm \times 0.435 mm, while the flat region is meshed with 0.435 mm $\, imes\,$ 0.456 mm elements. The residual stresses in the repaired composite obtained from the first numerical model (Section 4) are set as the initial stresses in the model. Displacement is applied to the end of the model similar to the experiments.

The interface between the adhesive layer and the composite base, as well as between the adhesive and the patch, is critical in determining the structural integrity of the repair system. To accurately capture the damage initiation and debonding of these interfaces, cohesive zone modeling (CZM) with a bilinear-shaped traction separation law is employed. According to this model, shown in Fig. 26, the traction increases linearly with separation between the surfaces up to the damage initiation traction limit. Beyond this point, the damage parameter increases gradually according to an evolution law until the failure criteria is reached and the surfaces are considered to be separated and debonded from each other.

The model used to define the model assumes an initial linear elastic behaviour. The CZM constitutive relation is defined as

$$\begin{pmatrix} \sigma_n \\ \tau_s \\ \tau_t \end{pmatrix} = \begin{pmatrix} K_n & 0 & 0 \\ 0 & K_s & 0 \\ 0 & 0 & K_t \end{pmatrix} \begin{pmatrix} \delta_n \\ \delta_s \\ \delta_t \end{pmatrix}$$
(19)

where, σ_n , τ_s and τ_t are the normal traction and the two shear tractions, respectively. K_n , K_s and K_t represent the corresponding stiffness. δ_n , δ_s and δ_t denote the corresponding separations.

Damage initiation under mixed-mode loading in the interface is captured using the quadratic nominal stress (QUADS) criterion, which is expressed as

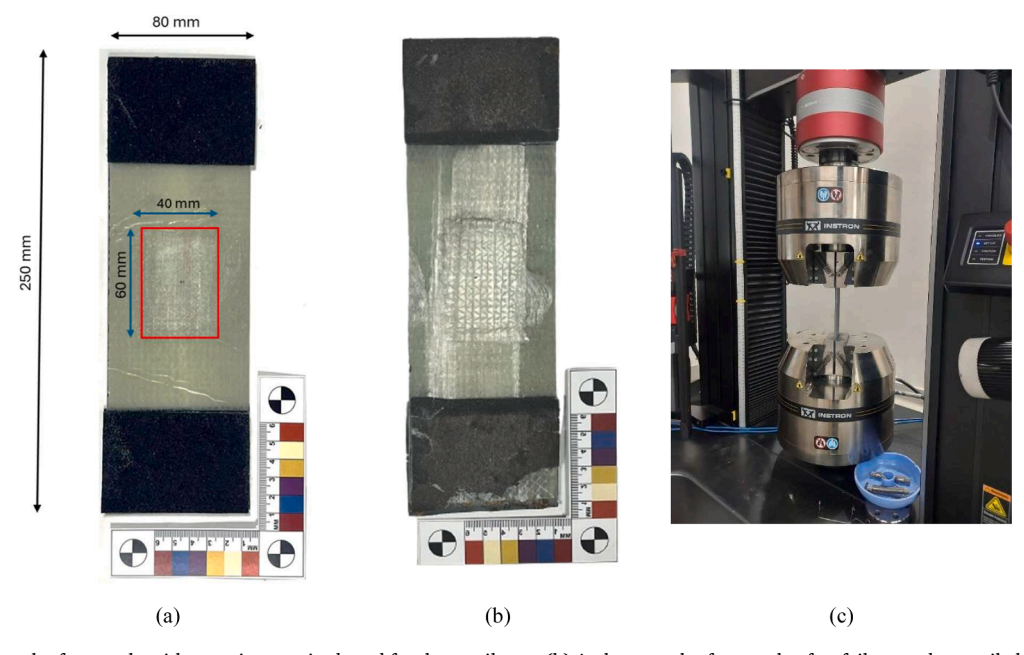


Fig. 22. (a) A photograph of a sample with a section repaired used for the tensile test (b) A photograph of a sample after failure under tensile loads (c) A photograph of the sample held between the grips in a UTM during the tensile test.

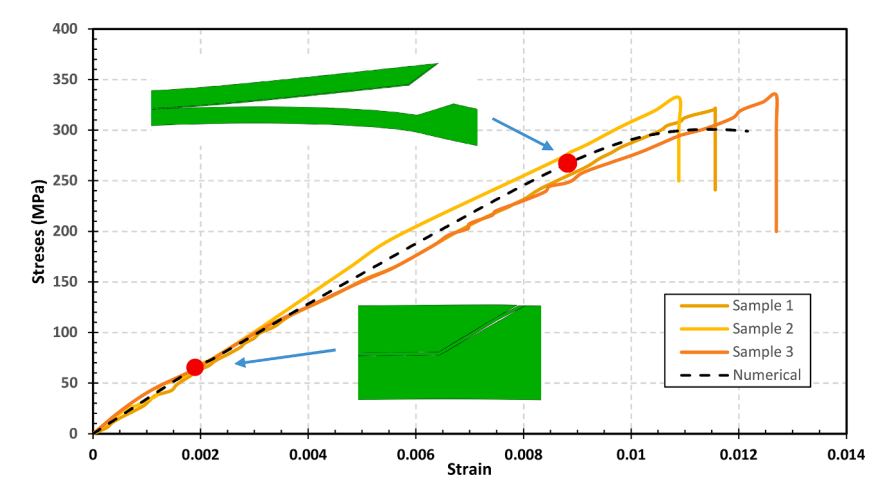


Fig. 23. Stress-strain curves for the scarf patch repaired samples.

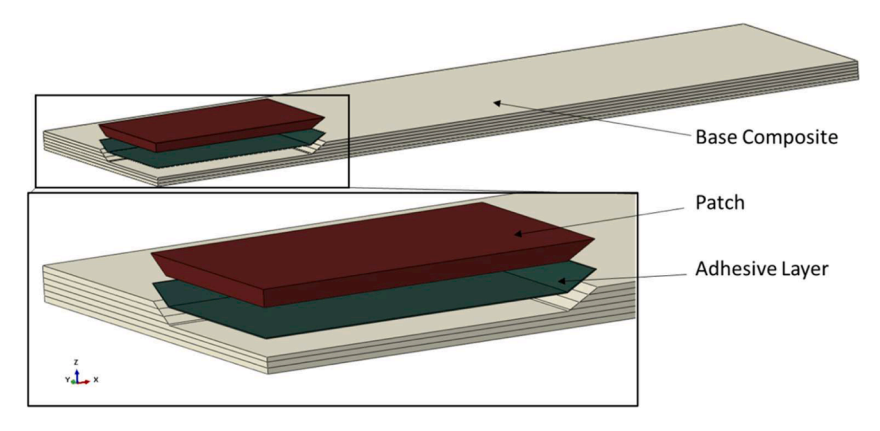


Fig. 24. Three-dimensional view of the scarf patch repair tensile model.

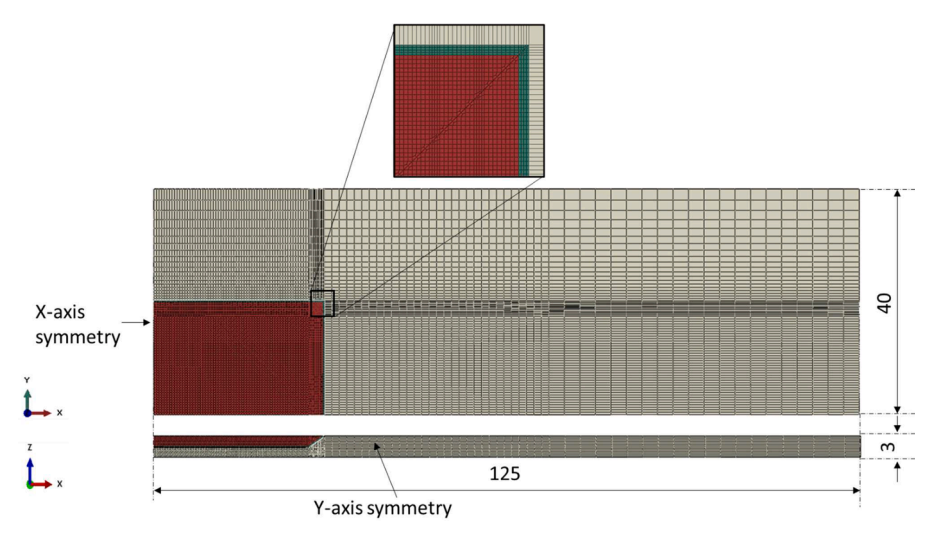


Fig. 25. Dimensions of the scarf patch repair tensile model.

$$\left\langle \frac{\sigma_n}{\sigma_{n_0}} \right\rangle^2 + \left(\frac{\tau_s}{\tau_{s_0}} \right)^2 + \left(\frac{\tau_t}{\tau_{t_0}} \right)^2 = 1 \tag{20}$$

 $\langle\cdot\rangle$ represents the Macaulay brackets, indicating that compressive stress (σ_n) does not cause damage. σ_{n_0} , τ_{s_0} and τ_{t_0} are the normal and shear traction limits at which damage initiation occurs.

Once the initiation criterion is met, the damage evolves linearly as

the separation increases, following the cohesive law until ultimate failure. The evolution of damage is defined based on the fracture energy, which is equal to the area under the traction-separation curve using the Benzeggagh-Kenane (B-K) fracture criterion which takes into account the interaction between the different modes of fracture energy and is given by

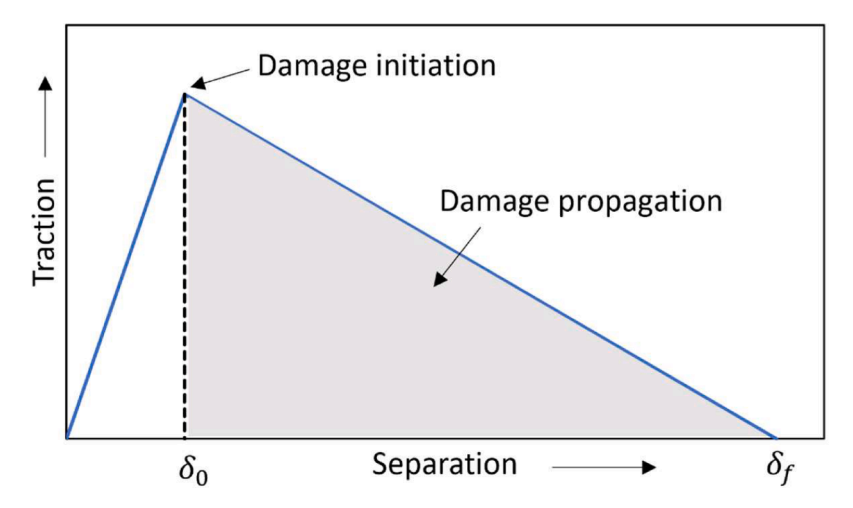


Fig. 26. A schematic representation of the bilinear traction separation law used in the model.

$$G^{c} = G_{n}^{c} + \left(G_{s}^{c} - G_{n}^{c}\right) \left(\frac{G_{s} + G_{t}}{G_{n} + G_{s} + G_{t}}\right)^{\eta}$$
(21)

where, G_n^c , G_s^c are the critical fracture energies which cause failures in the normal and shear directions and η is the material parameter and taken equal to 1.45. The parameters used in the model, such as the interface stiffness, interface strength, and fracture energy, are obtained from [29].

The composite itself is seen to show various modes of failure in the experiments including fiber breakage and matrix cracking. To model these failure mechanisms accurately, Hashin damage model is utilised. This model offers a comprehensive framework for predicting damage initiation and evolution in composite materials by distinguishing between different failure modes, particularly for fiber and matrix failure modes in both tension and compression. In this study, the Hashin damage criteria is implemented according to [30]. The criteria used are as follows:

i. Fiber tension (FT) failure criterion

$$F_{\rm ft} = \left(\frac{\sigma_1}{X_t}\right)^2 + \frac{\tau_{12}^2 + \tau_{13}^2}{S_t^2} \le 1 \tag{22}$$

where σ_1 is the longitudinal stress, X_t is the tensile strength of the fiber, τ_{12} , τ_{13} are the shear stresses in the respective planes and S_L is the longitudinal shear strength.

ii. Fiber compression (FC) failure criterion

$$F_{\rm fc} = \left(\frac{\sigma_1}{X_c}\right)^2 \le 1 \tag{23}$$

where X_c is the compressive strength of the fiber.

iii. Matrix tension (MT) failure criterion

$$F_{\text{mt}} = \left(\frac{\sigma_2 + \sigma_3}{Y_t}\right)^2 + \frac{\tau_{23}^2 - \sigma_2 \sigma_3}{S_T^2} + \frac{\tau_{21}^2 + \tau_{31}^2}{S_L^2} \le 1$$
 (24)

where σ_2 and σ_3 are transverse stresses, Y_t is the matrix tensile strength, τ_{23} , τ_{21} and τ_{31} are the shear stresses in the respective planes, and S_T is the transverse shear strength.

iv. Matrix compression (MC) failure criterion

$$F_{\text{mc}} = \left(\frac{Y_c^2}{4S_T^2} - 1\right) \left(\frac{\sigma_2 + \sigma_3}{Y_c}\right) + \left(\frac{\sigma_2 + \sigma_3}{2S_T}\right)^2 + \frac{\tau_{23}^2 - \sigma_2 \sigma_3}{S_T^2} + \frac{\tau_{21}^2 + \tau_{31}^2}{S_L^2}$$

$$< 1 \tag{25}$$

where Y_c is the matrix compressive strength.

Once the damage has initiated based on either of the above failure criteria, the damage evolution is implemented [30]. The numerical model is analysed in Abaqus. One important parameter which is studied is CSDMG which represents the overall value of the scalar damage variable, where a value of 1 indicates complete debonding. Fig. 27 shows the extent of debonding at the interface between the patch and the base composite at 25 % and 90 % of the failure load in the model. Red signifies that adhesive layer has debonded from the base composite while blue signifies that adhesive layer is still bonded with the base composite.

The evolution of damage within the composite is tracked as the load increases, allowing for the simulation of progressive failure and the assessment of the composite's residual strength after damage initiation. It is found that the base composite fails predominantly due to the matrix damage which starts at the corner of tapered region and propagates along the loading direction as shown in Fig. 28. This failure mode is consistent with the results observed in experiments as seen in Fig. 22(b) where the lighter shade above and below the repair patch are regions of extensive matrix damage.

Fig. 23 compares the predicted stress-strain curve with experimental data. The model predicts the initial stiffness and maximum stress well. The failure patterns seen in the numerical model are also similar to the ones seen in the experiments. As the patch begins to debond from the parent composite, the repaired laminate starts to bend under tensile loading. This bending, which is also seen in the actual tensile test, occurs due to a shift in the loading axis relative to central plane of composite, caused by the debonding of the patch. Fig. 23 also illustrates the point at which the patch begins to debond. In the model, debonding initiates at around 20 % of the maximum load and continues along the interface. Earlier studies have observed that although residual stresses have

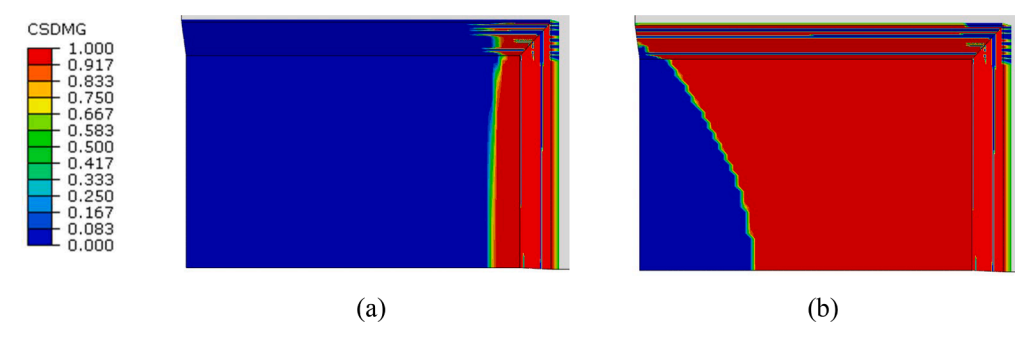


Fig. 27. Debonding at the interface between adhesive layer and base composite at (a) 25 % of the failure load and (b) 90 % of the failure load.

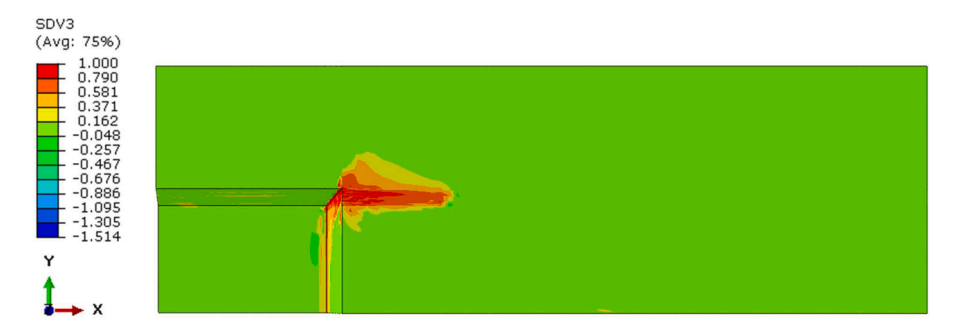


Fig. 28. Matrix damage distribution in the base composite at 97 % of the failure load.

minimal impact on tensile strength, they significantly affect fatigue performance [31]. However, studying this is beyond the scope of the current work and investigation into post-repair fatigue behaviour of composites will be undertaken separately in the future.

6. Conclusions

This paper examines scarf patch repair of composite laminates in the context of wind turbine blade repair. An orthotropic cure- and temperature-dependent Prony series-based viscoelastic model is used along with a hybrid analytical-numerical model to determine post-repair residual stresses in laminates. The model is used to estimate the residual stresses in the repaired laminate for various single- and two-stage temperature cycles. The results show that the repair parameters such as the temperature cycle can have significant effect on the residual stresses generated in the repaired laminate section. Higher cure temperatures result in higher post-repair residual stresses. The post-repair tensile behaviour of the repaired composite is also studied. Experiments show that damage initiates on the interface between the base composite and the repair patch and propagates along the interface until the repair patch is no longer able to carry loads. This ultimately leads to failure of the base composite. The average failure stress is 329 MPa. Numerical results corroborate the damage patterns and failure stresses seen in the experiments. In conclusion, the model proposed here simulates the repair process in composite laminates and its post-repair behaviour with the effects of residual stresses included. It provides a complete framework that is useful to determine and optimize the repair parameters in the wind turbine blade repair process.

CRediT authorship contribution statement

Ayush Varshney: Writing – original draft, Methodology, Investigation, Conceptualization. Daniel Paul: Writing – original draft, Methodology, Investigation, Conceptualization. Puneet Mahajan: Writing – review & editing, Supervision, Project administration, Funding acquisition. Leon Mishnaevsky: Writing – review & editing, Supervision, Project administration, Funding acquisition.

Declaration of competing interest

The authors declare the following financial interests/personal relationships which may be considered as potential competing interests:

Ayush Varshney reports financial support was provided by Indian Institute of Technology Delhi. Leon Mishnaevsky Jr. reports financial support and article publishing charges were provided by Technical University of Denmark. If there are other authors, they declare that they have no known competing financial interests or personal relationships that could have appeared to influence the work reported in this paper.

Data availability

Data will be made available on request.

Acknowledgements

The authors acknowledge the financial support of the Ministry of Foreign Affairs of Denmark via Danida grant 19-M02-DTU "Maintenance and repair strategy for wind energy development" (maintainergy.dk). LM is grateful to the Velux Foundation for its support of the project PREMISE "PREventing MIcroplastics pollution in SEa water from offshore wind" (https://premise.dtu.dk/).

References

- L. Mishnaevsky Jr., How to repair the next repair the next generation of wind turbine blades, Energies (Basel) 16 (23) (Nov. 2023) 7694, https://doi.org/ 10.3390/en16237694.
- [2] N. Kuthe, P. Mahajan, S. Ahmad, L. Mishnaevsky, Engineered anti-erosion coating for wind turbine blade protection: computational analysis, Mater Today Commun 31 (2022), https://doi.org/10.1016/j.mtcomm.2022.103362.
- [3] H. Li, C. Chen, T. Wang, L. Wang, Experimental study of stepped-lap scarf joint repair for spar cap damage of wind turbine blade in service, Appl Sci (Switzerland) 10 (3) (Feb. 2020), https://doi.org/10.3390/app10030922.
- [4] M.A. Caminero, S. Pavlopoulou, M. Lopez-Pedrosa, B.G. Nicolaisson, C. Pinna, C. Soutis, Analysis of adhesively bonded repairs in composites: damage detection and prognosis, Compos Struct 95 (Jan. 2013) 500–517, https://doi.org/10.1016/j. compstruct.2012.07.028.

- [5] D. Paul, A. Varshney, P. Mahajan, L. Mishnaevsky, Post-repair residual stresses and microstructural defects in wind turbine blades: computational modelling, Int J Adhes Adhes 123 (2023), https://doi.org/10.1016/j.ijadhadh.2023.103356.
- [6] D. Tzetzis, P.J. Hogg, Experimental and finite element analysis on the performance of vacuum-assisted resin infused single scarf repairs, Mater Des 29 (2) (2008) 436–449, https://doi.org/10.1016/j.matdes.2007.01.002.
- [7] C. Sun, et al., Mechanical behaviour of composite laminates repaired with a stitched scarf patch, Compos Struct 255 (Jan. 2021), https://doi.org/10.1016/j. compstruct.2020.112928.
- [8] L. Mishnaevsky, "Root causes and mechanisms of failure of wind turbine blades: overview," 2022. doi: 10.3390/ma15092959.
- [9] A. Courtois et al., "Viscoelastic behavior of an epoxy resin during cure below the glass transition temperature: characterization and modeling," 2019. doi: 10.11 77/0021998318781226.
- [10] Y.K. Kim, S.R. White, Stress relaxation behavior of 3501-6 epoxy resin during cure, Polym Eng Sci 36 (23) (1996), https://doi.org/10.1002/pen.10686.
- [11] A. Gillani, "Development Of material model subroutines for linear and nonlinear response of elastomers," Electronic Thesis and Dissertation Repository. 5837., 2018.
- [12] S. Blanco, H. You, T.W. Kerekes, G.J. Yun, Cure-induced residual stress buildup and distortions of CFRP laminates with stochastic thermo-chemical and viscoelastic models: experimental verifications, Mech Adv Mater Struct 29 (19) (2022), https:// doi.org/10.1080/15376494.2021.1877376.
- [13] P.J. Halley, M.E. Mackay, Chemorheology of thermosets an overview, Polym Eng Sci 36 (5) (1996), https://doi.org/10.1002/pen.10447.
- [14] Y. Ledru, G. Bernhart, R. Piquet, F. Schmidt, L. Michel, Coupled visco-mechanical and diffusion void growth modelling during composite curing, Compos Sci Technol 70 (15) (2010), https://doi.org/10.1016/j.compscitech.2010.08.013.
- [15] M. Ivankovic, L. Incarnato, J.M. Kenny, L. Nicolais, Curing kinetics and chemorheology of epoxy/anhydride system, J Appl Polym Sci 90 (11) (2003), https://doi.org/10.1002/app.12976.
- [16] M. Agrawal, M. Gupta, R.T. Durai Prabhakaran, P. Mahajan, A comparative study of static and fatigue performance of glass and basalt fiber reinforced epoxy composites, Polym Compos 45 (4) (Mar. 2024) 3551–3565, https://doi.org/ 10.1002/pc.28008.
- [17] M. Gupta, R.T.D. Prabhakaran, P. Mahajan, Non-linear material characterization and numerical modeling of cross-ply basalt/epoxy laminate under low velocity impact, Polym Test 84 (Apr. 2020), https://doi.org/10.1016/j. polymertesting.2020.106349.

- [18] P. Lux, A.G. Cassano, S.B. Johnson, M. Maiaru, S.E. Stapleton, Adhesive curing cycle time optimization in wind turbine blade manufacturing, Renew Energy 162 (Dec. 2020) 397–410, https://doi.org/10.1016/j.renene.2020.08.043.
- [19] A.K. Kaw, Mechanics of composite materials, CRC press, 2005.
- [20] J. Dai, S. Xi, D. Li, Numerical analysis of curing residual stress and deformation in thermosetting composite laminates with comparison between different constitutive models, Materials (Basel) 12 (4) (Feb. 2019), https://doi.org/10.3390/ mail.2040572.
- [21] O.G. Kravchenko, S.G. Kravchenko, R.B. Pipes, Chemical and thermal shrinkage in thermosetting prepreg, Compos Part A Appl Sci Manuf 80 (Jan. 2016) 72–81, https://doi.org/10.1016/j.compositesa.2015.10.001.
- [22] Z. Yuan, et al., Evolution of curing residual stresses in composite using multi-scale method, Compos B Eng 155 (Dec. 2018) 49–61, https://doi.org/10.1016/j. compositesb.2018.08.012.
- [23] A. Yebi, B. Ayalew, Optimal layering time control for stepped-concurrent radiative curing process, J Manuf Sci Eng Trans ASME 137 (1) (2015), https://doi.org/ 10.1115/1.4029023.
- [24] Y. Zhao, X. Jiang, Q. Zhang, Q. Wang, Numerical simulation of thermal performance of glass-fibre-reinforced polymer, in: IOP conference series: materials science and engineering, Institute of Physics Publishing, Nov. 2017, https://doi. org/10.1088/1757-899X/245/2/022016.
- [25] S. Chava, S. Namilae, Continuous evolution of processing induced residual stresses in composites: an in-situ approach, Compos Part A Appl Sci Manuf 145 (Jun. 2021), https://doi.org/10.1016/j.compositesa.2021.106368.
- [26] T.Y.F. Chen, et al., "Use of digital image correlation method to measure bio-tissue deformation,", Coatings 2021 11 (8) (Aug. 2021) 924, https://doi.org/10.3390/ COATINGS11080924. Page 924, vol. 11.
- [27] J. Nairn and P. Zoller, "Matrix solidification and the resulting residual thermal stresses in composites," 1985.
- [28] Y. Baig, X. Cheng, H.J. Hasham, M. Abbas, W.A. Khan, Failure mechanisms of scarf-repaired composite laminates under tensile load, J Braz Soc Mech Sci Eng 38 (7) (Oct. 2016) 2069–2075, https://doi.org/10.1007/s40430-015-0460-z.
- [29] V.H. Truong, B.S. Kwak, R. Roy, J.H. Kweon, Cohesive zone method for failure analysis of scarf patch-repaired composite laminates under bending load, Compos Struct 222 (Aug. 2019), https://doi.org/10.1016/j.compstruct.2019.110895.
- [30] M.R.T. Arruda, M. Trombini, A. Pagani, Implicit to explicit algorithm for ABAQUS standard user-subroutine UMAT for a 3D hashin-based orthotropic damage model, Appl Sci (Switzerland) 13 (2) (Jan. 2023), https://doi.org/10.3390/app13021155.
- [31] U. Thakre, A. Tewari, Effect of residual-stress evolution during curing process on fatigue-life of fiber-reinforced polymers, J Reinf Plast Compos 42 (1–2) (Jan. 2023) 65–81, https://doi.org/10.1177/07316844221101573.